Progress In Electromagnetics Research, Vol. 168, 133–143, 2020

Dual-Mode Hyperspectral Bio-Imager with a Conjugated Camera for Quick Object-Selection and Focusing

Xinli Yao[1, 2], Shuo Li[1, 2], and Sailing He[1, 2, 3, *]

Abstract—A dual-mode hyperspectral imager using field of view scanning needs no moving macro parts. It could work in dual-mode (macro imaging and micro imaging) and is equipped with a conjugated camera for quick object-selection and focusing. By adjusting the imaging lens and achieving the image clarity on the conjugated camera, we could find the correct location and focusing of the ROIs simultaneously instead of inefficiently checking the hyperspectral image after the whole scanning process. The whole system was applied to the study of spectral characteristics of blood oxygen in human hands and the microscopic identification of algae, showing a great potential of clinical and marine applications of our system.

1. INTRODUCTION

Hyperspectral imaging, which combines spectroscopy and digital imaging, has been widely used in remote sensing, medicine, agriculture, food detection and other fields [1–6]. The most common working modes of hyperspectral imaging are point scan, push-broom and staring imaging. Push-broom hyperspectral imaging technology has a good compromise between spatial resolution, spectral resolution and acquisition time [7], and is a relatively mature technique. However, push-broom modes require moving macro parts, which limits its imaging range and compact size. Moreover, it is difficult to quickly localize and focus on the ROIs. It mainly depends on the experience of the operator to focus on the line spectral image [8, 9], and it often requires push broom imaging several times to determine the imaging position, which is very time consuming.

Light could pass through a certain thickness of biological tissue, and various substances in biological tissue will absorb light at different wavelengths, so the reflectance spectra of tissues or organs contains relevant useful information [10–12]. With hyperspectral imaging, non-invasive detection of human tissues or organs can be realized. Liu et al. used hyperspectral images and the support vector machine to analyze medical tongue images and obtain much better tongue segmentation results [13]. Hadox et al. found that retinal hyperspectral imaging may predict brain amyloid beta load [14]. Cai et al. studied the blood concentration in human hands using spectral images at 580 nm [15]. Hyperspectral information also provides valuable information for the identification of normal and cancerous tissues, diagnosis of diseases, etc. [2, 16].

Red tide and other marine disasters seriously damage or destroy marine ecological environments [17, 18]. Some red tide algae are toxic to other marine organisms and human life and should be monitored. Hyperspectral detection of algae uses remote sensing by satellites at an altitude of about 800 km and local remote sensing by aircraft below 3 km [19–21]. The identification of common algae mainly relies on morphological characterization with high magnification microscope [22, 23]. In addition, the spectral information can also provide a basis for algae identification. Mehrubeoglu et al. used

Received 3 August 2020, Accepted 29 October 2020, Scheduled 21 November 2020

* Corresponding author: Sailing He (sailing@zju.edu.cn).

[1] Centre for Optical and Electromagnetic Research, Chinese National Engineering Research Center for Optical Instruments, Zhejiang University, Hangzhou 310058, China. [2] Ningbo Research Institute, Zhejiang University, Ningbo 315100, China. [3] JORCEP, School of Electrical Engineering, Royal Institute of Technology, SE-100 44 Stockholm, Sweden.

hyperspectral data and some linear spectral unmixing algorithm to analyze mixed algal cultures containing two algae of known volumes at a macro level [24]. Volent et al. mounted a hyperspectral imager (400–700 nm) on a stereo-microscope and compared the absorption, transmittance and reflectivity of algae to distinguish in vivo optical signatures of different pigment groups [25]. Wei et al. developed a hyperspectral microscopic imaging system and used the Fisher algorithm to identify the species of three microalgae [26].

However, all of the above imaging methods require a moving platform whether it is for macro imaging or micro imaging and don't have quick object-selection and focusing in practical operation. In this paper, we built a dual-mode hyperspectral imager based on field of view scanning, which could realize scanning in the staring state (no moving macro part) and work in two modes: macro imaging and micro imaging by changing the imaging lens and relay lens. In addition, our system is equipped with a conjugated camera for gray-scale imaging, which shares the same imaging lens with the hyperspectral camera. By adjusting the imaging lens and observing the image on the conjugated camera, we can judge whether the ROIs selection and focusing are correct. This method no longer requires a complete scanning processor are construction of the hyperspectral image to confirm the selection of ROIs, thus realizing quick object-selection and focusing. The system was applied to sensing of bio-samples, including the spectral characteristics of blood oxygen in human hand (macro imaging) and identification of algae (micro imaging), which shows the great potential for clinical and marine applications.

2. METHODS

The schematic of the dual-mode hyperspectral bio-imager is presented in Fig. 1. The key component of the system lies in the galvanometer mirror, which transforms the traditional push-brooms can into the field of view scan. The beam splitter is used to divide the optical path into two channels: gray-scale imaging channel and hyperspectral imaging channel. The final image planes of the two channels are conjugated and share the same imaging lens. The imaging lens images the scene on the entrance pupil, which is between an aspheric achromatic lens (AAL-1, Edmund, #49-665) and the imaging lens. After being collimated by aspheric achromatic lens AAL-1, the light of the image on the entrance pupil reaches the beam splitter, 10% of the light is reflected into the gray-scale imaging channel (conjugated camera), and then focused on the CMOS-1 (ZWO, ASI120MMmini) by another aspheric achromatic lens (AAL-2). 90% of the light is transmitted into the hyperspectral imaging channel. The collimated light (after AAL-1) is reflected by the galvanometer mirror and form an image through an aspheric

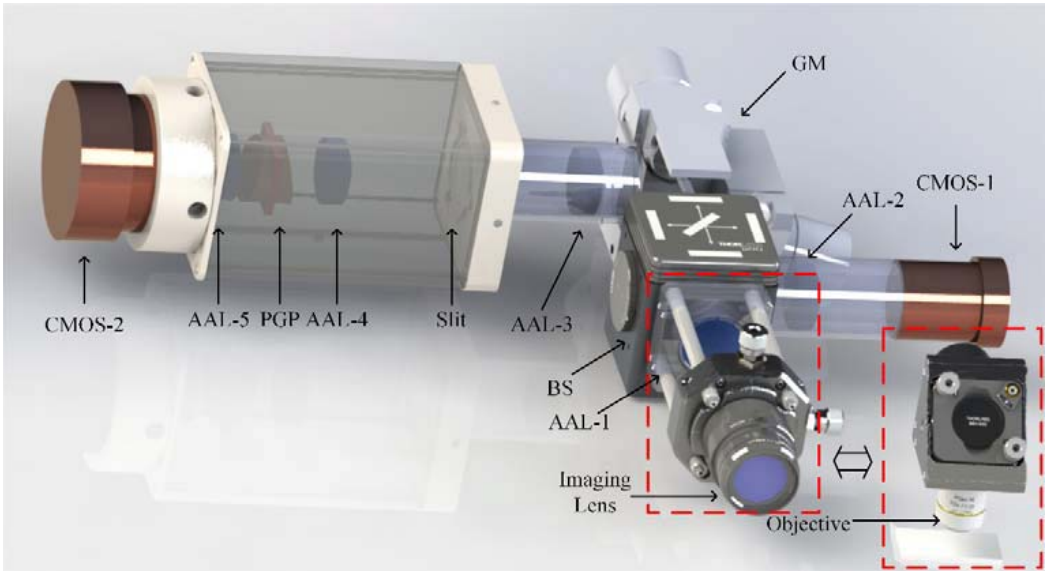

Figure 1. Schematic diagram of the dual-mode hyperspectral bio-imager. AAL: aspheric achromatic lens; BS: beam splitter; GM: galvanometer mirror; PGP: prism-grating-prism.

achromatic lens (AAL-3) on a plane containing a slit (50 µm), which is the relay plane of entrance pupil just like CMOS-1. Only a line region of the image will pass through the slit, and the light in the line region will be collimated by an aspheric achromatic lens (AAL-4) and reach a prism-grating-prism (PGP) pair for dispersion. After being dispersed by PGP, the light of the line region is expanded in the spectral dimension and focused on the CMOS-2 (ZWO, ASI174MM) by an aspheric achromatic lens (AAL-5). In general, a push-broom imaging spectrometer can obtain hyperspectral images by collecting different line regions of the same image, and the moving part is indispensable. In this paper, we use the galvanometer mirror (Thorlab, GVS012) to change the angle of the incident light continuously, so that the image moves on the relay image plane (slit), which is also equivalent to collecting different line regions of the same image, so as to realize scanning imaging in the staring state. Since CMOS-1 (for gray-scale imaging) and CMOS-2 (for hyperspectral imaging) are conjugated and the two channels share the same imaging lens, we can quickly allocate and focus the ROIs by observing the image clarity on the conjugated gray-scale imaging camera.

An infinity-corrected optical system is a common optical structure of modern microscopy. A light beam emitted from an object passes through the microscopic objective which does not form an image and enters as a collimated beam in the tube lens which forms an intermediate image. In the above hyperspectral imaging system, image relay is realized by two aspheric achromatic lenses, and the beam between the two lenses is collimated. Therefore, the imaging lens and AAL-1 in Fig. 1 can be replaced by the microscope objective, and the aspheric achromatic lens (AAL-2 or AAL-3) in the subsequent optical path can be used as the tube lens to convert the system into a microscope and realize dual-mode imaging.

For an imaging spectrometer detector, one dimension records the spatial data from a line region of image (serves as the spatial axis), and the other dimension records the spectral data (serves as the spectral axis), as shown in the coordinate axis in Fig. 2(a). Before the application of homemade imaging spectrometer, the pixel index of the spectral axis needs to be converted into wavelength values. The spectral image of a mercury lamp can be obtained by irradiating the slit of imaging spectrometer with the mercury lamp, as shown in Fig. 2(a). The mercury lamp can emit multiple extremely narrow spectral lines. In this paper, we choose 404.6 nm, 435.8 nm, 546.1 nm, 578.0 nm, 750.4 nm, 763.5 nm and 772.4 nm spectral lines for wavelength calibration, and the corresponding pixel indices are 54, 147, 646, 553, 1023, 1058, 1082, respectively. The relationship between the wavelength and pixel index can be fitted by polynomial [27]. In this paper, the third-order polynomial is selected for wavelength calibration, and the fitted curve is shown in Fig. 2(b), whose wavelength range is 387–821 nm. Fig. 2(c) is the spectral curve of the mercury lamp after wavelength calibration, in which the full width at half maximum of the spectral line of 546.1 nm is about 3.5 nm.

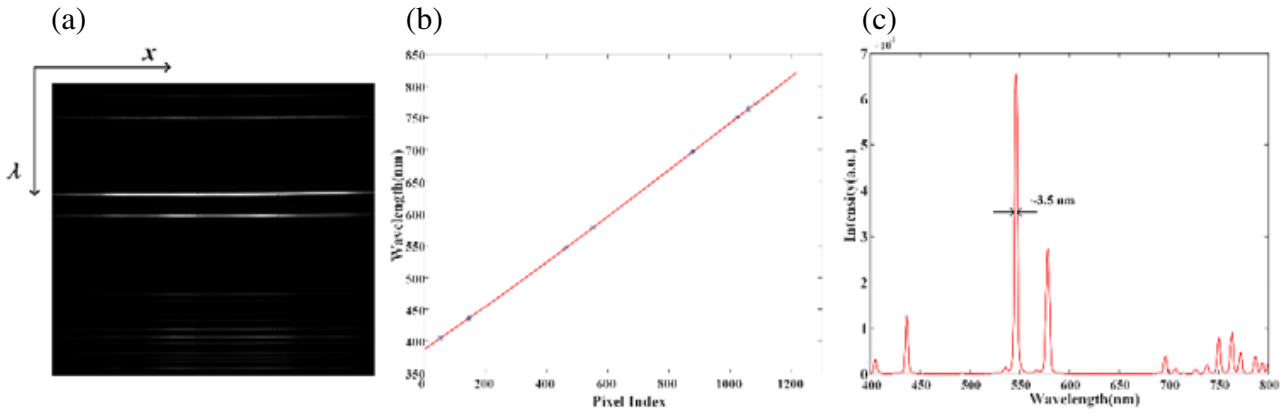

Figure 2. (a) The spectral image of mercury lamp captured by the CMOS-2 (the vertical axis is the spectral axis; the horizontal axis is a spatial axis); (b) The relationship between the wavelength and pixel index fitted by third-order polynomial; (c) The spectral curve of the mercury lamp measured by our homemade imaging spectrometer after wavelength calibration.

3. RESULTS AND DISCUSSION

3.1. Spatial Consistency Verification and Imaging Test

By changing the voltage of galvanometer mirror to deflect at different angles to image the line regions at different positions, the system can complete hyperspectral imaging. In order to understand the spatial correspondence to different voltages, we image the checkerboard with our hyperspectral camera. The two-dimensional spatial images are shown in Fig. 3(a), which are obtained by the y-direction movement of the x-line scanning corresponding to the voltage range of 1.8–2.3 V, 2.3–2.8 V, 2.8–3.3 V, 3.3–3.8 V. As can be seen from Fig. 3(a), these four spatial images occupy 2.5 grids in the y-direction. In order to quantify this spatial data, the intensity values of the corresponding pixel points are taken out at the blue line position in Fig. 3(a) and drawn in Fig. 3(b). The pixel points occupied by the five white

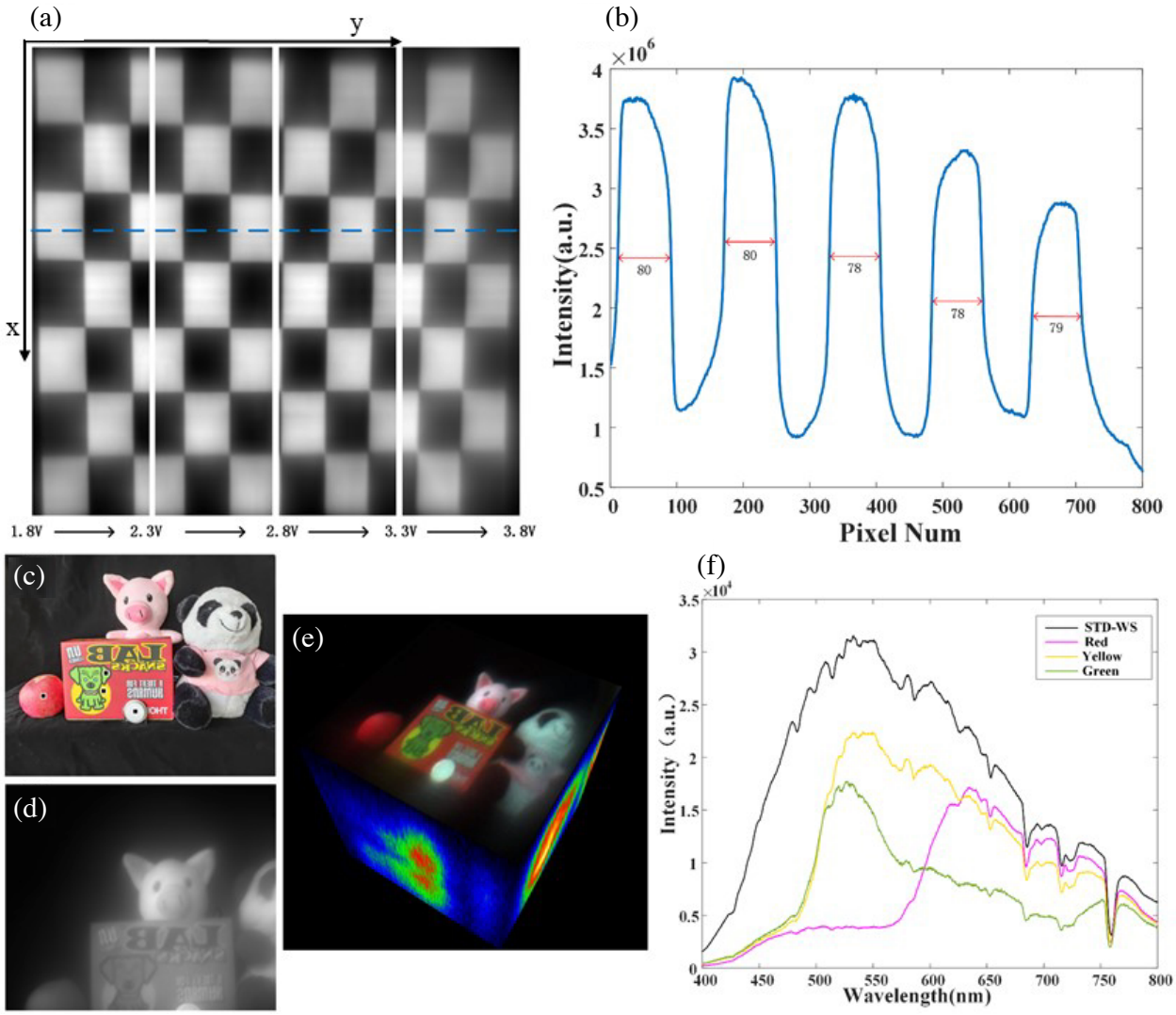

Figure 3. (a) The two-dimensional spatial images of the checkerboard, with the y-direction movement corresponding to the voltage range of 1.8–2.3 V, 2.3–2.8 V, 2.8–3.3 V, 3.3–3.8 V, are obtained by our hyperspectral camera; (b) The intensity values of the corresponding pixel points of the blue line position in Fig. 3(a); (c) Photo of the test scene; (d) Image of the test scene taken by the gray-scale camera; (e) Hyperspectral cube image of the test scene taken by our hyperspectral camera; (f) Reflected spectra of the four black-dot regions in Fig. 3(c).

grids are 80, 80, 78, 78, 79 respectively from left to right, which shows that the spatial position of the hyperspectral imaging system based on galvanometer mirror is basically consistent in different fields of view, without shape distortion.

In order to verify the imaging capability of the system, including hyperspectral imaging and gray-scale imaging, we image the test scene in Fig. 3(c) under sunlight. Fig. 3(d) is an image taken by the conjugated camera, and Fig. 3(e) is a hyperspectral cube image captured by the hyperspectral camera, which is obtained by rendering 200 spectral image sequences with the spectral module in Python. The color of the two-dimensional spatial image in Fig. 3(d) is determined by the intensities at wavelengths of 650 nm, 530 nm and 450 nm in the hyperspectral cube as the R, G, B components, which is consistent with the color in Fig. 3(c). From the comparison of Fig. 3(d) and Fig. 3(e), we see that the field of view of hyperspectral image is larger than that of gray-scale image, because the scanning field of view corresponding to 1.8–3.8 V is larger than the field of view of gray-scale imaging camera.

The reflected spectra are extracted and plotted (Fig. 3(f)) for four regions in Fig. 3(c) (indicated by black dots), which are standard white plate (STD-WS), red part on the apple, yellow and green patterns on the carton. All the observed spectra show many hollows on the spectral line, especially at 760 nm. This is because the scene is illuminated by sunlight, which gets partially absorbed by water vapor and gas when the sunlight passes through the atmosphere [28, 29]. The reflected spectra of the three color dot regions have peaks in the corresponding color bands. All of the above shows the imaging ability and spectral acquisition accuracy of our system.

3.2. Spectral Characteristics of Blood Oxygen in Human Hand

To study the spectral characteristics of blood oxygen in human hands, we image a real hand and a printed photo of a human hand as an example of a fake hand. As shown in Fig. 4(a), a real human hand is on the left and a printed photo of a human hand is on the right (as a fake hand). To eliminate the unwanted influence due to different illuminations and detectors, the spectra were corrected with white reference. The acquired raw spectra can be corrected with the following equation:

$$R(\lambda) = \frac{R_o(\lambda) - D}{R_w(\lambda) - D} \tag{1}$$

where $R(\lambda)$ is the reflectance spectrum; $R_o(\lambda)$ is the raw spectrum reflected by the object; $R_w(\lambda)$ is the spectrum of the standard white plate; and D is the dark noise of the detectors.

We extract the reflectance spectra of the palm part in the hyperspectral cube and average it over a small area centered at each spatial pixel. The averaged reflectance spectra of the real palm and fake palm are shown in Fig. 4(b). The spectrum of the real palm shows a "W" shape in the band of 500–600 nm, with absorption peaks at 540 nm and 576 nm. This is because oxygenated hemoglobin (HbO_2) in the blood absorbs strongly at 540 nm and 576 nm [30], resulting in a decrease in reflectivity. The reflectivity peak bands of the printed fake palm are 440 nm, 520 nm and 650 nm, which correspond to the blue, green and red respectively. This is because the printed fake palm is printed with a RGB primary color ink. Through the above analysis, we can distinguish between real and fake hands using spectral characterization and see the presence of HbO_2.

In order to further study the blood oxygen absorption characteristics of human hand, the reflectance spectrum is converted into the absorbance spectrum through the following equation:

$$A(\lambda) = -\lg(R(\lambda)) \tag{2}$$

where $A(\lambda)$ is the absorbance spectrum, and $R(\lambda)$ is the reflectance spectrum. Then the absorbance spectra of the palm and finger were extracted and plotted in Fig. 4(c), showing prominent peaks at 540 nm and 576 nm. In addition, there is also an absorption peak at about 420 nm. This is the characteristic absorption of hemoglobin and porphyrin complexes in the UV visible region [31], known as the Soret band, which has blue shift or red shift depending on different binding substances. Fig. 4(c) shows that the absorbance of finger region of the human hand in each absorption band of HbO_2 is greater than that of palm region. This is because finger's blood oxygen saturation can reach 98% (measured with a blood oxygen meter in advance), while the palm's blood oxygen saturation is lower than the finger's. We extracted the corresponding intensity image at 576 nm from the hyperspectral cube, and calculated its absorbance intensity image through Equations (1) and (2). As shown in Fig. 4(d), the

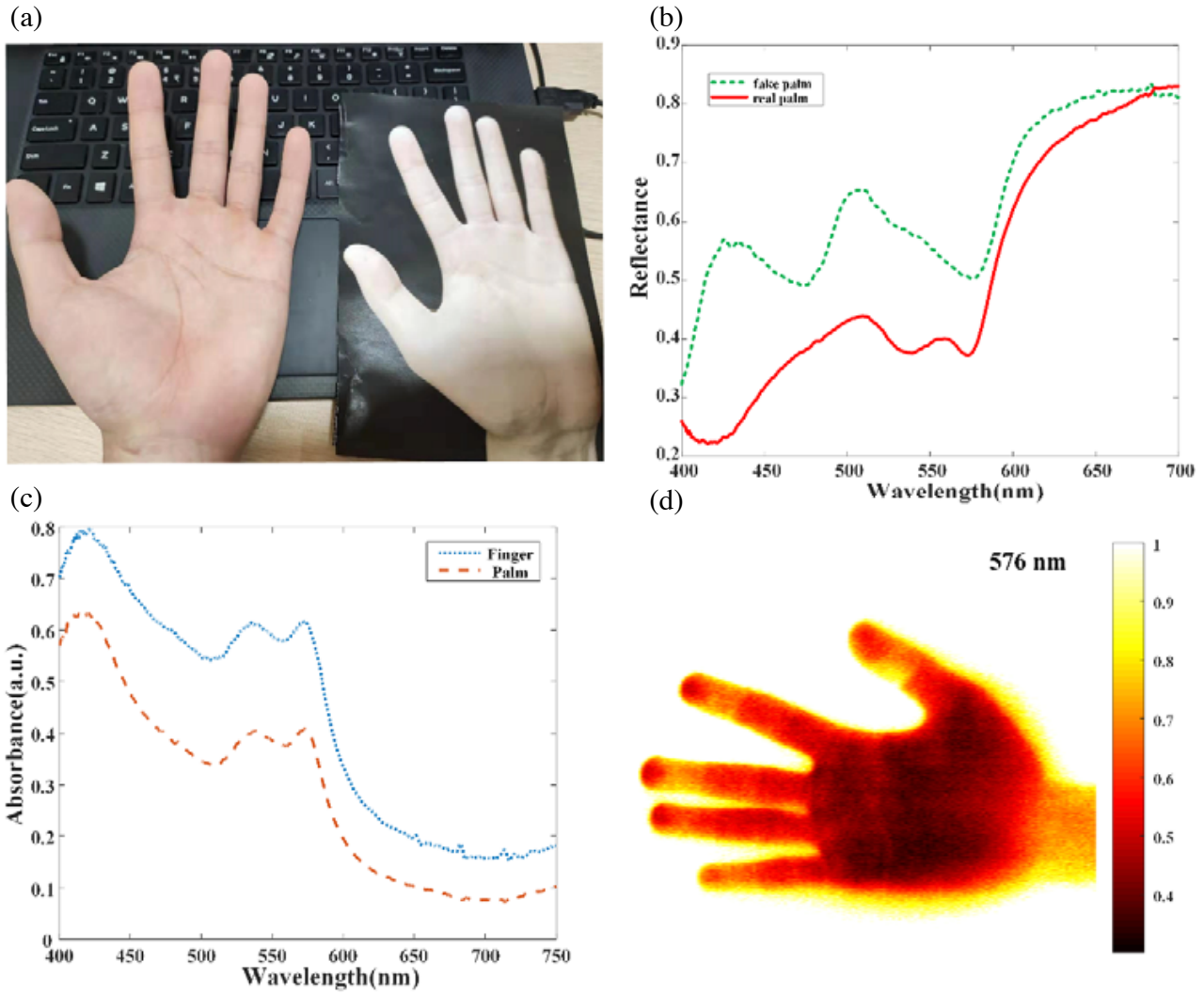

Figure 4. (a) Photo of a real human hand and a printed photo of a human hand (as a fake hand); (b) Averaged reflectance spectra of the fake palm and real palm; (c) Absorbance spectra averaged over a finger region and a palm region of the human hand; (d) Absorbance intensity image at the 576 nm band.

numerical absorbance value of the palm region is smaller than that at the finger region. Hence, the absorbance intensity at 576 nm can provide a qualitative assessment of the distribution of blood oxygen concentration.

The above analysis is for oxygenated hemoglobin, which is the main existing state of hemoglobin in human hands. Hemoglobin also has a state without bound oxygen, due to the aerobic consumption of human tissue. The absorbance spectrum of such hemoglobin is distinct from oxygenated hemoglobin. According to the data given in Reference [30], the molar extinction coefficient curves of hemoglobin and oxygenated hemoglobin are drawn in Fig. 5(a). From the curve in Fig. 5(a), we can see that there are absorption peaks at 416 nm, 540 nm, and 576 nm of oxygenated hemoglobin, which is consistent with our above conclusion; the absorption peaks of hemoglobin are at 433 nm and 556 nm, and the wavelength corresponding to the Soret band has a red shift compared with oxygenated hemoglobin. We imaged a normal hand and a hand with poor blood circulation. The hand with poor blood circulation is achieved by tightening a bandage on the wrist, and the blood oxygen in the hand will be exhausted after a certain amount of time, and the spectral characteristics of the hand will be changed due to the reduction of oxygenated hemoglobin to hemoglobin.

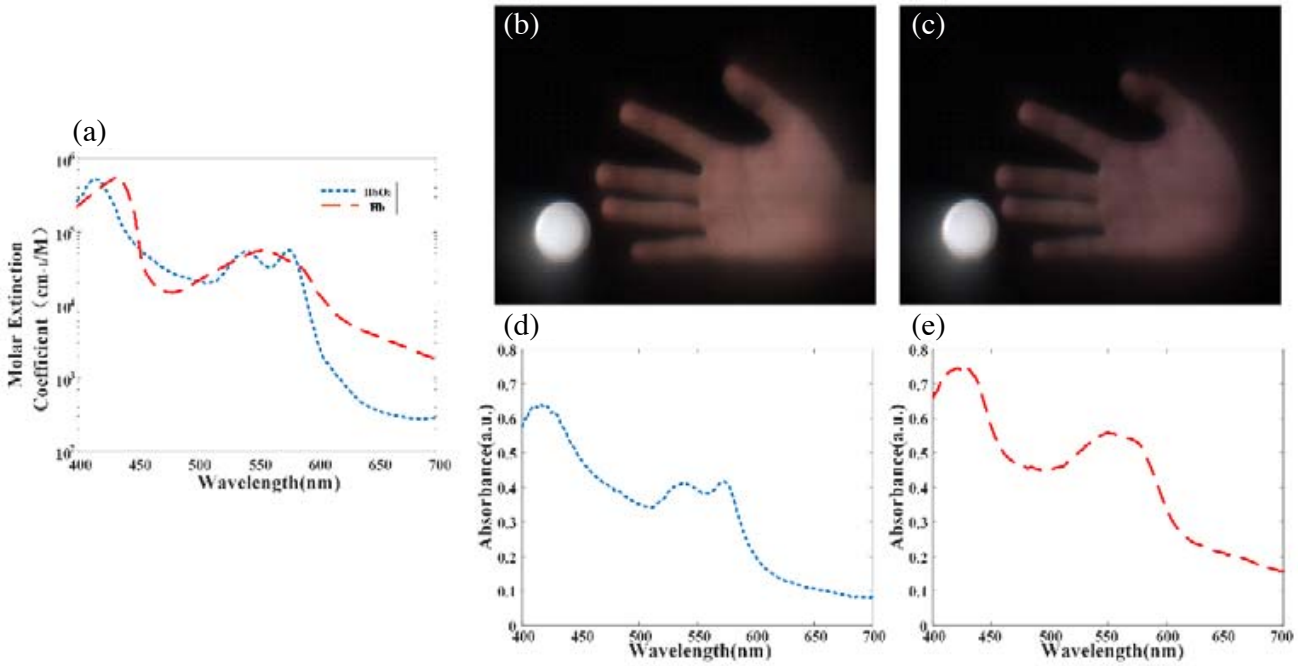

Figure 5. (a) Molar extinction coefficient curves of hemoglobin and oxygenated hemoglobin; (b) RGB rendering image of a normal hand; (c) RGB rendering image of a hand with poor blood circulation; (d) Absorbance spectrum of a normal hand; (e) Absorbance spectrum of a hand with poor blood circulation.

The hyperspectral rendered images of a normal hand and a hand with poor blood circulation are shown in Figs. 5(b)–(c) (the white circular object is a standard white board). Figs. 5(d)–(e) show the absorbance spectra of a normal hand and a hand with poor blood circulation, respectively. In Fig. 5(d) the peaks of the absorbance spectrum of the normal hand are at 420 nm, 540 nm and 576 nm, which are consistent with the peaks of molar extinction coefficient of oxygenated hemoglobin. The peaks of the absorbance spectrum of the hand with poor blood circulation are 430 nm and 552 nm, which are consistent with the peaks of molar extinction coefficient of hemoglobin. The above results demonstrate that the spectral characteristics of the hand would change with the hemoglobin state when the blood circulation of the hand is restricted. The comparison of Fig. 5(b) and Fig. 5(c) shows that the color of the normal hand is different from that of the hand with poor blood circulation, and the hand with poor blood circulation is darker. However, due to differences of skin color, it is difficult to judge the blood circulation state of a hand directly through RGB imaging. By using the hyperspectral imaging technology, the state of hemoglobin can be analyzed based on the spectral dimension, which demonstrates the potential for the preliminary diagnosis of some vascular occlusive diseases.

3.3. Microscopic Hyperspectral Imaging for Algae

As mentioned in Section 2, the system can work in two hyperspectral imaging modes (macro imaging and micro imaging). Here, we used the micro imaging with a 10× objective to observe five microalgae and one macroalgae. We put five kinds of microalgae (Chaetoceros, Synechocystis, Chlorella, Phaeocystis and Chlamydomonas reinhardtii; all their sizes are less than 10 µm) into a glass dish and detected the reflectance spectra. The RGB rendering images and the averaged reflectance spectra corresponding to the five microalgae are shown in Figs. 6(a)–(j). It is difficult to distinguish the microalgae directly by color in RGB images because of their small size and weak reflection. In contrast, their spectral characteristics are different and can be classified. In general, the microscopic classification of microalgae requires the observation of morphology by high magnification microscope (about 100×). However, when our system is operated in the micro imaging mode, an objective with low magnification (instead of a high magnification microscope) can be used to distinguish the microalgae according to the spectral

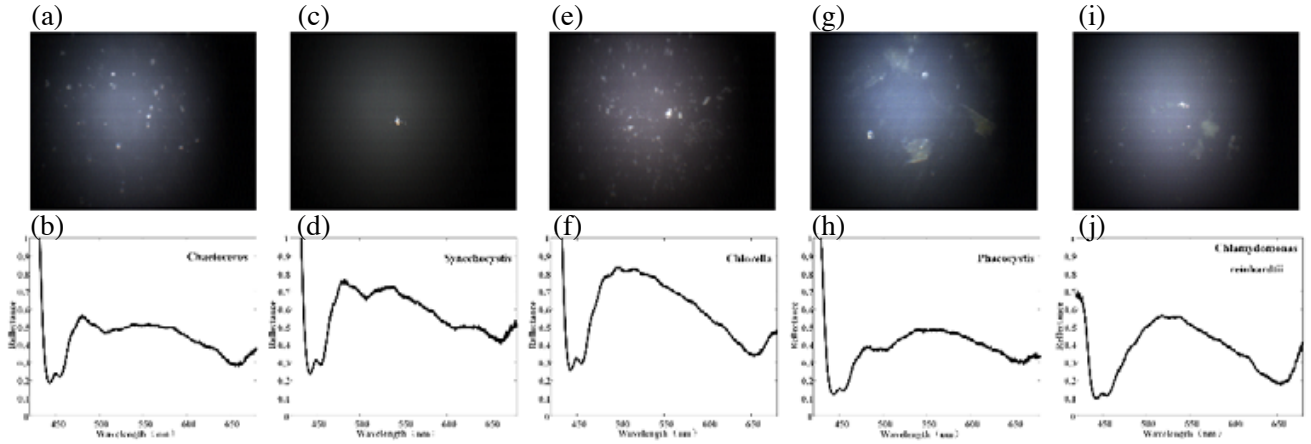

Figure 6. (a) RGB rendering image of Chaetoceros; (b) Reflectance spectrum of Chaetoceros; (c) RGB rendering image of Synechocystis; (d) Reflectance spectrum of Synechocystis; (e) RGB rendering image of Chlorella; (f) Reflectance spectrum of Chlorella; (g) RGB rendering image of Phaeocystis; (h) Reflectance spectrum of Phaeocystis; (i) RGB rendering image of Chlamydomonas reinhardtii; (j) Reflectance spectrum of Chlamydomonas reinhardtii.

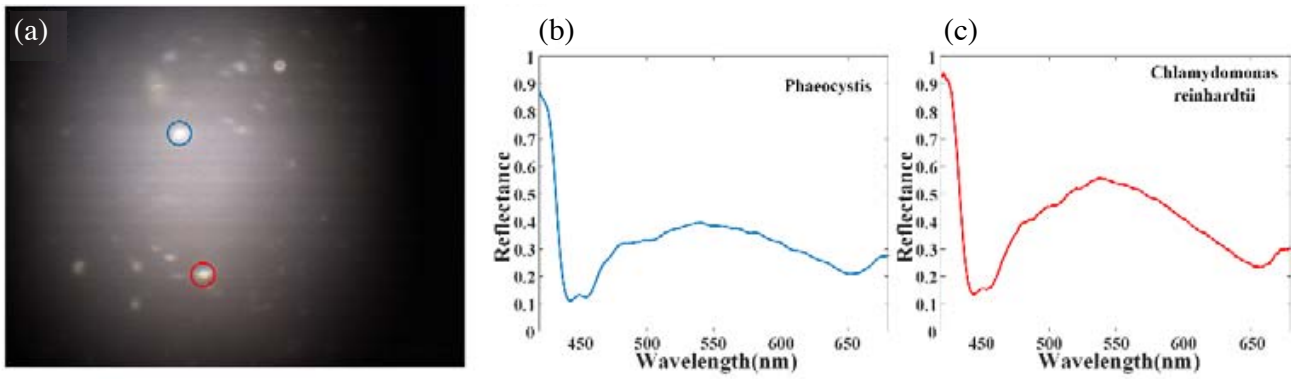

Figure 7. (a) RGB rendering image of mixed microalgae; (b) Reflectance spectra averaged over the blue circle region in Fig. 6(a); (c) Reflectance spectra averaged over the red circle region in Fig. 6(a).

information.

We mixed Phaeocystis and Chlamydomonas reinhardtii, put them into a glass dish, and obtained their hyperspectral cube. The RGB rendering image of mixed microalgae is shown in Fig. 7(a). The averaged reflectance spectra of microalgae corresponding to the blue and red circles in Fig. 7(a) are plotted in Figs. 7(b)–(c). It is hard to distinguish the species of microalgae from their morphology or color in Fig. 7(a). From the trend and absorption peak of spectral curve, using the spectral curve obtained in Fig. 6, it can be determined that the microalgae corresponding to Fig. 7(b) is Phaeocystis, and the microalgae corresponding to Fig. 7(c) is Chlamydomonas reinhardtii.

In addition, we also cultivated large Chlamydomonas reinhardtii (macroalgae, particle size is about 100 μm) for microscopic hyperspectral imaging. The RGB rendering image is shown in Fig. 8(a). Due to the large particle size, the color of macroalgae is obvious, and flagella can be observed. There are some red scattering points which indicate the eyespot that falls off Chlamydomonas, as shown in the red box in Fig. 8(a). The eyespot allows Chlamydomonas to swim towards the light for photosynthesis. The reflectance spectra of the cell wall and eyespot of the macroalgae were extracted and normalized, as shown in Fig. 8(b). The spectrum of eyespot is similar to that of cell wall, with absorption peak at 660 nm and reflection peak at 525 nm, which is a characteristic of chlorophyll. The reflectance of

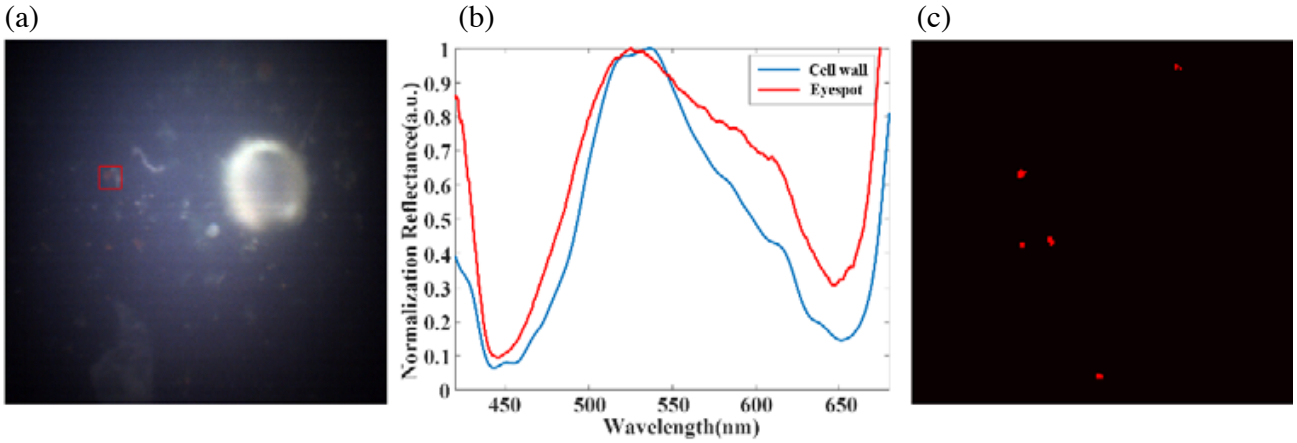

Figure 8. (a) RGB rendering image of a large Chlamydomonas reinhardtii; (b) Normalized reflectance spectra of the cell wall and eyespot of the large Chlamydomonas reinhardtii; (c) Image showing the locations of eyespots.

the eyespot at 575–625 nm region is higher than that of the cell wall, which is due to the presence of red photosensitive protein in the eyespot. The intensity image of hyperspectral cube at 600 nm band was extracted, and threshold segmentation and mathematical morphology processing are carried out, as shown in Fig. 8(c). The red dot in Fig. 8(c) shows the locations of the eyespot. Through the appropriate processing of hyperspectral cube, the position of eyespot can be accurately localized. Further spectral analysis of Chlamydomonas could obtain more biologically specific information, such as the spectral characteristics of photosensitive proteins in eyespots, which provides some supporting information for the subsequent treatment of blindness.

4. CONCLUSION

In this paper, we have developed a compact hyperspectral system with no large moving parts by using a galvanometer mirror to scan the field of view. The system has two channels, namely, the gray-scale imaging and hyperspectral imaging. The cameras of the two channels are conjugated, and thus the system can quickly locate the ROIs and get focused there by observing the gray-scale camera. The system can successfully distinguish the real hand and fake hand, qualitatively obtain the distribution of blood oxygen concentration, and distinguish the difference between the normal hand and the hand with poor blood circulation. It shows the great potential application in the real or fake face recognition, blood oxygen quantitative calculation and vascular disease detection.

We have also used a low magnification objective to replace the front imaging lens and a relay lens. The whole system then functions as a microscope with higher dimensionality of information than ordinary microscopes. By applying this system, we have obtained hyperspectral cubes of five different kinds of microalgae and distinguished them by hyperspectral information without relying on morphology or any high magnification objective. In addition, the hyperspectral imaging of large Chlamydomonas reinhardtii has also been carried out, and the spectral characteristics of its eyespot and cell wall have been analyzed.

Funding

This work is supported by National Key Research and Development Program of China (#2018YFC1407503), Ningbo Science and Technology Project (No. 2018B10093), the Fundamental Research Funds for the Central Universities (2019FZA5002), National Natural Science Foundation of China (11621101), Science and Technology Development Plan Project of Changshu (No. CS201806). The authors are grateful to Dr. Julian Evans for helpful discussions.

Disclosures

The authors declare that there are no conflicts of interest related to this article.

REFERENCES

1. Cloutis, E. A., "Review Article: Hyperspectral geological remote sensing: Evaluation of analytical techniques," *International Journal of Remote Sensing*, Vol. 17, 2215–2242, 1996.
2. Lu, G. and B. Fei, "Medical hyperspectral imaging: A review," *Journal of Biomedical Optics*, Vol. 19, 010901, 2014.
3. Li, J., W. Jiang, X. Yao, F. Cai, and S. He, "Fast quantitative fluorescence authentication of milk powder and vanillin by a line-scan hyperspectral system," *Appl. Opt.*, Vol. 57, 6276, 2018.
4. Yao, X., F. Cai, P. Zhu, H. Fang, J. Li, and S. He, "Non-invasive and rapid pH monitoring for meat quality assessment using a low-cost portable hyperspectral scanner," *Meat Science*, Vol. 152, 73–80, 2019.
5. Jiang, W., J. Li, X. Yao, E. Forsberg, and S. He, "Fluorescence hyperspectral imaging of oil samples and its quantitative applications in component analysis and thickness estimation," *Sensors*, Vol. 18, 4415, 2018.
6. Johnsen, G., "Kelp forest mapping by use of airborne hyperspectral imager," *J. Appl. Remote Sens.*, Vol. 1, 011503, 2007.
7. Boldrini, B., W. Kessler, K. Rebner, and R. Kessler, "Hyperspectral imaging: A review of best practice, performance and pitfalls for inline and online applications," *Journal of Near Infrared Spectroscopy*, Vol. 20, 438, 2012.
8. Sigernes, F., M. Syrjäsuo, R. Storvold, J. Fortuna, M. E. Grøtte, and T. A. Johansen, "Do it yourself hyperspectral imager for handheld to airborne operations," *Opt. Express*, Vol. 26, 6021, 2018.
9. Saager, R. B., A. N. Dang, S. S. Huang, K. M. Kelly, and A. J. Durkin, "Portable (handheld) clinical device for quantitative spectroscopy of skin, utilizing spatial frequency domain reflectance techniques," *Review of Scientific Instruments*, Vol. 88, 094302, 2017.
10. Bhandari, A., B. Hamre, Ø. Frette, K. Stamnes, and J. J. Stamnes, "Modeling optical properties of human skin using Mie theory for particles with different size distributions and refractive indices," *Opt. Express*, Vol. 19, 14549–14567, 2011.
11. Li, H., C. Zhang, and X. Feng, "Monte Carlo simulation of light scattering in tissue for the design of skin-like optical devices," *Biomed. Opt. Express*, Vol. 10, 868, 2019.
12. Yousefi, S., J. Qin, and R. K. Wang, "Super-resolution spectral estimation of optical micro-angiography for quantifying blood flow within microcirculatory tissue beds in vivo," *Biomed. Opt. Express*, Vol. 4, 1214, 2013.
13. Liu, Z., J. Yan, D. Zhang, and Q.-L. Li, "Automated tongue segmentation in hyperspectral images for medicine," *Appl. Opt.*, Vol. 46, 8328, 2007.
14. Hadoux, X., F. Hui, and J. K. H. Lim, "Non-invasive in vivo hyperspectral imaging of the retina for potential biomarker use in Alzheimer's disease," *Nature Communications*, Vol. 10, 4227, 2019.
15. Cai, F., D. Wang, M. Zhu, and S. He, "Pencil-like imaging spectrometer for bio-samples sensing," *Biomed. Opt. Express*, Vol. 8, 5427, 2017.
16. Panasyuk, S. V., S. Yang, D. V. Faller, D. Ngo, R. A. Lew, J. E. Freeman, and A. E. Rogers, "Medical hyperspectral imaging to facilitate residual tumor identification during surgery," *Cancer Biology & Therapy*, Vol. 6, 439–446, 2007.
17. Yang, L., K. J. Han, and Z. Y. Chen, "Dynamic relationship between economic growth in coastal and marine disaster losses: 1989–2011," *Scientia Geographica Sinica*, School of Business, Shandong University, 2015.
18. Christie-Oleza, J. A., D. Sousoni, M. Lloyd, J. Armengaud, and D. J. Scanlan, "Nutrient recycling facilitates long-term stability of marine microbial phototroph-heterotroph interactions," *Nat. Microbiol.*, Vol. 2, 17100, 2017.

19. Lou, X. and C. Hu, "Diurnal changes of a harmful algal bloom in the East China Sea: Observations from GOCI," *Remote Sensing of Environment*, Vol. 140, 562–572, 2014.
20. Choi, J. K., Y. J. Park, B. R. Lee, J. Eom, J.-E. Moon, and J.-H. Ryu, "Application of the Geostationary Ocean Color Imager (GOCI) to mapping the temporal dynamics of coastal water turbidity," *Remote Sensing of Environment*, Vol. 146, 24–35, 2014.
21. Andrefouet, S., C. Payri, E. J. Hochberg, C. Hu, M. J. Atkinson, and F. E. Mullerkarger, "Use of *in situ* and airborne reflectance for scaling-up spectral discrimination of coral reef macroalgae from species to communities," *Marine Ecology Progress Series*, Vol. 283, 161–177, 2004.
22. Wang, D. Z., L. Lin, H. F. Gu, L. L. Chan, and H. S. Hong, "Comparative studies on morphology, ITS sequence and protein profile of *Alexandrium tamarense* and A. *catenella* isolated from the China Sea," *Harmful Algae*, Vol. 7, 106–113, 2008.
23. Hindák, F. and A. Hindáková, "Morphology and taxonomy of some rare chlorococcalean algae (Chlorophyta)," *Biologia*, Vol. 63, 781–790, 2008.
24. Mehrubeoglu, M., M. Teng, and P. Zimba, "Resolving mixed algal species in hyperspectral images," *Sensors*, Vol. 14, 1–21, 2013.
25. Volent, Z., G. Johnsen, and F. Sigernes, "Microscopic hyperspectral imaging used as a bio-optical taxonomic tool for micro- and macroalgae," *Appl. Opt.*, Vol. 48, 4170, 2009.
26. Wei, L., K. Su, S. Zhu, H. Yin, Z. Li, Z. Chen, and M. Li, "Identification of microalgae by hyperspectral microscopic imaging system," *Spectroscopy Letters*, Vol. 50, 59–63, 2017.
27. Cho, J., P. J. Gemperline, and D. Walker, "Wavelength calibration method for a CCD detector and multichannel fiber-optic probes," *Applied Spectroscopy*, Vol. 49, 1841–1845, 1995.
28. Koutchmy, S., F. Baudin, Sh. Abdi, L. Golub, and F. Sèvre, "New deep coronal spectra from the 2017 total solar eclipse," *Astronomy and Astrophysics*, Vol. 632, A86, 2019.
29. Minnaert, M. G. J., "The solar spectrum (L)," *Practical Work in Elementary Astronomy*, 123–125, Springer, 1969.
30. Kollias, N. and W. Gratzer, "Tabulated molar extinction coefficient for hemoglobin in water," Vol. 5, 150–161, Wellman Laboratories, Harvard Medical School, Boston, 1999.
31. Rimington, C., "Spectral-absorption coefficients of some porphyrins in the Soret-band region," *Biochemical Journal*, Vol. 75, 620–623, 1960.